ACS OMEGA

Open Access

http://pubs.acs.org/journal/acsodf

Article

Design and Development of a Self-Supporting ZIF-62 Glass MOF Membrane with Enhanced Molecular Sieving for High H_2 Separation Efficiency

Hamidreza Mahdavi, Joseph F. Olorunyomi, Nathan T. Eden, Cara M. Doherty, Durga Acharya, Stefan J.D. Smith,* Xavier Mulet,* and Matthew R. Hill*

Cite This: *ACS Omega* 2025, 10, 7441−7451

Read Online

ACCESS | Metrics & More | Article Recommendations | Supporting Information

ABSTRACT: The purpose of this study was to design and develop a self-supporting glass MOF membrane (GMM) including its design, fabrication under different heat treatment temperatures, analysis of its physical−chemical properties, and assessment of its separation performance. Glass MOFs preserve metal−ligand bonding structures similar to their crystalline counterparts, providing intrinsic gas separation properties alongside the benefits of amorphous materials, including reduced grain boundaries and ease of processing. In this work, ZIF-62 was melted and then cooled to fabricate GMMs using vitrification to enhance molecular sieving. This study systematically examines the impact of varying thermal treatment temperatures (400−475 °C) on the physical and chemical transformations of GMMs, revealing their effects on the porosity, defect formation, and molecular sieving performance through advanced characterization techniques (e.g., solid-state nuclear magnetic resonance (^{13}C NMR), X-ray photoelectron spectroscopy (XPS), He pycnometry, and positron annihilation lifetime spectroscopy (PALS)). The optimal GMM exhibits an impressive separation performance, particularly for H_2 separation. The GMM at 4 bar and 25 °C exhibited He, H_2, CO_2, N_2, and CH_4 gas permeations of 576.37, 509.23, 146.07, 3.45, and 2.28 barrer, respectively. The ideal selectivities of H_2/CH_4, CO_2/N_2, CO_2/CH_4, H_2/N_2, and H_2/CO_2 gas pairs were 223.47, 42.37, 64.10, 147.71, and 3.49, respectively, which significantly exceed earlier reported values for ZIF-62 membranes, demonstrating the significant potential for GMMs as high-performance molecular sieve membranes, particularly for H_2 separation. This work by optimizing the vitrification process through systematic temperature control highlights GMM's ability to achieve high selectivity and permeability, positioning it as a promising candidate for industrial gas separation applications.

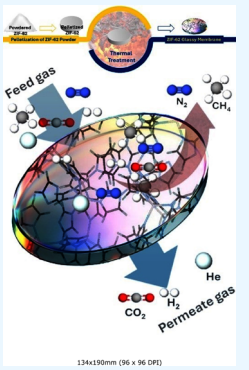

INTRODUCTION

Polycrystalline membranes are considered one of the most innovative emerging technologies due to their ease of use, environmental friendliness, low capital investment, and low energy consumption.[1−6] These membranes can be made of organic or inorganic materials.[7,8] However, inorganic membranes seem to be more suitable as a result of their high durability, good thermal and chemical stability, narrow and well-defined pore size distribution, and antiaging properties.[9,10] On the other hand, metal−organic frameworks (MOFs) as a new generation of porous materials with molecular sieving properties have emerged as a promising candidate for manufacturing high-performance membranes.[11,12] MOFs are particularly promising as additives in membrane fabrication due to their chemical and structural versatility, molecular-size pores, and high tunability compared to other porous materials.[13−21]

However, when it comes to the fabrication of self-standing membranes, MOFs face similar challenges as inorganic materials such as intercrystallite and grain boundary defects that can compromise selectivity and increase permeability inconsistencies.[22,23] Indeed, the size sieving effect is extremely sensitive to imperfections; even minor intercrystal and grain boundary defects can create inconsistent pore sizes that significantly decrease selectivity and simultaneously increase permeability. To address these issues, researchers have investigated a variety of post-treatment methods such as surface polymerization and oriented tertiary growth aimed to minimize intercrystal and grain boundary defects.[24−27] Despite the progress made, these methods have not entirely addressed the issues of polycrystalline membranes. Conversely, glass MOFs have attracted significant attention for their potential to address these challenges and deliver effective membrane separation performance.[28−35]

Generally, a glass MOF is fabricated by melting crystalline MOF through the solid−liquid phase transition to the liquid state above its melting temperature (T_m) followed by rapid cooling of the resulted liquid MOF below its glass transition temperature (Tg), known as the vitrification process.[29,36] In both liquid and glass phases, porosity was preserved.[37,38] In fact,

Received: January 15, 2025
Revised: February 2, 2025
Accepted: February 5, 2025
Published: February 10, 2025

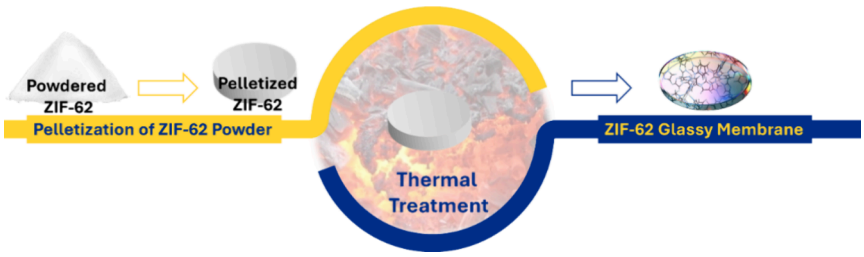

Figure 1. Schematic of the fabrication of GMMs.

the solid−liquid−glass transition expands their ability to be processed and shaped compared to that of crystallized MOFs, making them particularly versatile. Furthermore, glass MOFs have greater capabilities of extending structural diversity and properties, which are not available in traditional organic, inorganic, and metallic glasses.[39−41] The intercrystal and grain boundary defects can be reduced in the liquid MOF phase, allowing for the formation of glass MOFs with high separation performances.[42−45] One of the most promising candidates among MOFs is ZIF-62, known for its high glass-forming ability (GFA) and low melting temperature. In addition, ZIF-62 experiences only one melting process before decomposition and does not undergo any intermediate recrystallization, which prevents intercrystal and grain boundary defects.[29,46−48] These abilities are ascribed to its unique structure and properties, which include high viscosity, low fragility, and resistance to crystallization, making it ideal for creating a highly selective, stable, defect-free glass MOF membrane (GMM) for gas separation applications.[46,47] However, GMMs must exhibit mechanical robustness, maintain long-term stability, and attain high selectivity and permeability (meeting or exceeding the Robeson upper bound trade-off) to be industrially viable. These benchmarks ensure that the membranes can operate cost-effectively and efficiently under operational conditions.[4,49]

Wang et al. have reported the in situ fabrication of a glass ZIF-62 membrane supported on alumina and silica for mixed gas separations. Although this study demonstrates significant advancements, including the elimination of intercrystalline defects via the vitrification process and high separation performance, it suffers from limitations in the optimization of membrane preparation and the depth of characterization.[42] Moreover, supported membranes face the drawback of restricted mass transfer often caused by potential incompatibility between the support layer and the active components. In contrast, self-standing membranes eliminate this limitation, significantly enhancing the mass transfer process.[50] Moreover, recent studies demonstrated that glass ZIF-62 has a fracture toughness (K_{Ic}) of approximately 0.1 MP·m$^{0.5}$, which is lower than that of the majority of brittle oxide glasses.[51] Meanwhile, it exhibits a Young's modulus between approximately 3.2 and 6.6 GPa and a hardness ranging from 0.37 to 0.7 GPa, depending on the synthesis method, with melt-quenched glass ZIF-62 typically exhibiting the higher end of these ranges. These values suggest that the glasss ZIF-62 is softer and more mechanically flexible than oxide-based glasses.[32,51] Despite its relatively low toughness and hardness, glass ZIF-62 exhibits a brittle-to-ductile transition, which enables up to 35% plastic deformation, which is an uncommon property for a glass. This unique combination of moderate Young's modulus and increased ductility indicates significant promise for durable applications necessitating a balance of flexibility and mechanical strength.[52,53] Recent studies also indicated that glass ZIF-62 synthesized using melt-quenching removes grain boundaries, which are often sites for defect formation and chemical degradation. This structural integrity is crucial for preserving long-term stability in harsh conditions.[54,55] For example, in the absence of grain boundaries, glass ZIF-62 exhibits resistance to chemical degradation and maintains its structural integrity even when exposed to corrosive agents such as H_2O, Na^+, and Cl^-.[54] Its amorphous structure also contributes to thermal stability, enabling it to preserve integrity throughout diverse temperature conditions.[55] The defect-free characteristics of glass ZIF-62 enhance its effectiveness in gas separation applications, exhibiting durable, antiaging capabilities with consistent performance for durations of up to 10 days and, in some cases such as glass TIF-4, extending to 10 months.[36,42,43,45,55−57] On the other hand, studies showed that glass ZIF-62 has considerable promise as a gas separation membrane owing to its adjustable structure and composition.[21,35] The porous structure of glass ZIF-62 can be modified by changing the metal nodes (e.g., Co, Zn), hence affecting gas affinity and separation performance.[58] The mixed-metal node glass ZIF-62 exhibits improved CO_2/CH_4 selectivity, making it appropriate for natural gas purification and carbon capture applications.[56,58] Furthermore, glass ZIF-62 has the capability to fabricate composites with crystalline materials such as ZIF-7 or ZIF-8 as well as with polymers such as cellulose acetate (CA) and polymers with intrinsic microporosity (PIM), therefore modifying porosity and gas affinities to target specific separations.[21,36,59,60] This composite glass ZIF-62 exhibits improved selectivity and permeability for C_2H_6/C_2H_4, a valuable separation in petrochemical processes.[35] These composite membranes exhibit a promising capacity to meet or even exceed the Robeson upper bound trade-off for various gas separations, including CO_2/CH_4, H_2/N_2, and H_2/CO_2.[61,62]Although existing studies have highlighted the promising properties of glass ZIF-62 and its potential for gas separation applications, there is a limited understanding of how these properties vary under different heat treatment temperatures.

The purpose of this paper is to present the systematic design and fabrication of self-supporting GMMs along with a comprehensive analysis of the physical−chemical properties and structural transformations of GMMs under different heat treatment temperatures (400−475 °C). This enables the identification of an optimal fabrication temperature that results in an exceptional gas separation performance. Therefore, ZIF-62 has been used to fabricate GMMs as a result of its wide melting range. The GMMs have been fabricated by melting ZIF-62 and then cooling it. The characterization properties of GMMs have been assessed using an extensive suite of advanced characterization techniques including scanning electron microscopy (SEM), thermogravimetric analysis (TGA), differential scanning calorimetry (DSC), powder X-ray diffraction (PXRD), Fourier-transform infrared spectroscopy (FTIR), solid-state

https://doi.org/10.1021/acsomega.5c00466
ACS Omega 2025, 10, 7441−7451

nuclear magnetic resonance (^{13}C NMR), X-ray photoelectron spectroscopy (XPS), low-pressure gas sorption, He pycnometry, and positron annihilation lifetime spectroscopy (PALS) that provide a deeper understanding of the structural transformations, pore structure, and defect formation mechanisms in GMMs. Finally, the optimal GMM separation performance has been evaluated using several gases, including He, H_2, CO_2, N_2, and CH_4. Based on the study findings, GMM presented impressive separation performance, particularly in H_2 separation, demonstrating significant potential for achieving both high selectivity and permeation, or, in other words, ultimate gas separation.

EXPERIMENTAL SECTION

The ZIF-62 nanoparticles were synthesized using the techniques outlined in the Supporting Information (SI) Section S2. As shown in Figure 1, a series of GMMs were fabricated by pelletizing and then sintering the synthesized ZIF-62 at different temperatures.[42] Each sample is denoted as GMM-T, where T indicates the sintering temperature. For example, a sample that has been sintered to a temperature of 400 °C is referred to as GMM-400 °C. Several characterization techniques were used to analyze the fabricated GMMs in terms of physical transformations, thermal stability, structural and framework changes, and evaluation of pore structure and architecture. This analysis provides a comprehensive understanding of the structural, chemical, and physical characteristics of the GMMs and enables the identification of the optimal sample. The performance of the optimal GMM was assessed by evaluating their gas permeabilities and pair gas selectivities at 4 bar and 25 °C.

RESULTS AND DISCUSSION

The ZIF-62 GMMs were fabricated by initially pelletizing synthesized and activated ZIF-62 powder followed by heating under a vacuum to temperatures (T's) above 400 °C, around its T_m. Figure 2 shows surface and cross-sectional SEM images along with photographs of ZIF-62 and the GMMs obtained at different T's from 400 to 475 °C. The morphology of the hexagonal prism-like crystals of ZIF-62 (Figure 2a) was significantly deformed due to the gradual melting of the particles, leading to the formation of GMM-400 at 400 °C (Figure 2b). At increasing annealing T (415−445 °C), the deformed particles were further formed into a continuous phase with smooth surfaces and more uniform and defect-free cross sections for GMM-415, GMM-430, and GMM-445 (Figures 2c−e). The photographs of the GMMs show that they appear dark yellow and are translucent with rough surfaces. At higher annealing T (460 and 475 °C), the surface and cross-section morphologies of the GMMs shown in Figure 2f,g indicate the formation of mesopores and defects, with additional macroscopic bubbles forming visible in the inset photographs.

Based on the TGA data shown in Figure 3a, ZIF-62 demonstrates the highest weight percentage decrease followed by GMM-400 °C to GMM-475 °C. The rate of mass reduction exhibits a gradual decrease as the sintering temperatures increase, and the reduction beyond 445 °C becomes less significant. Moreover, DSC was used to gain further an insight into the transformation of ZIF-62 crystals into the GMMs. The DSC trace shown in Figure 3b indicates the T_g and T_m of ZIF-62 occurring at 327 and 443 °C, respectively. GMMs could not be fabricated below 443 °C, and as T approaches 550 °C, the gradual decomposition of ZIF-62 was observed. In reference to

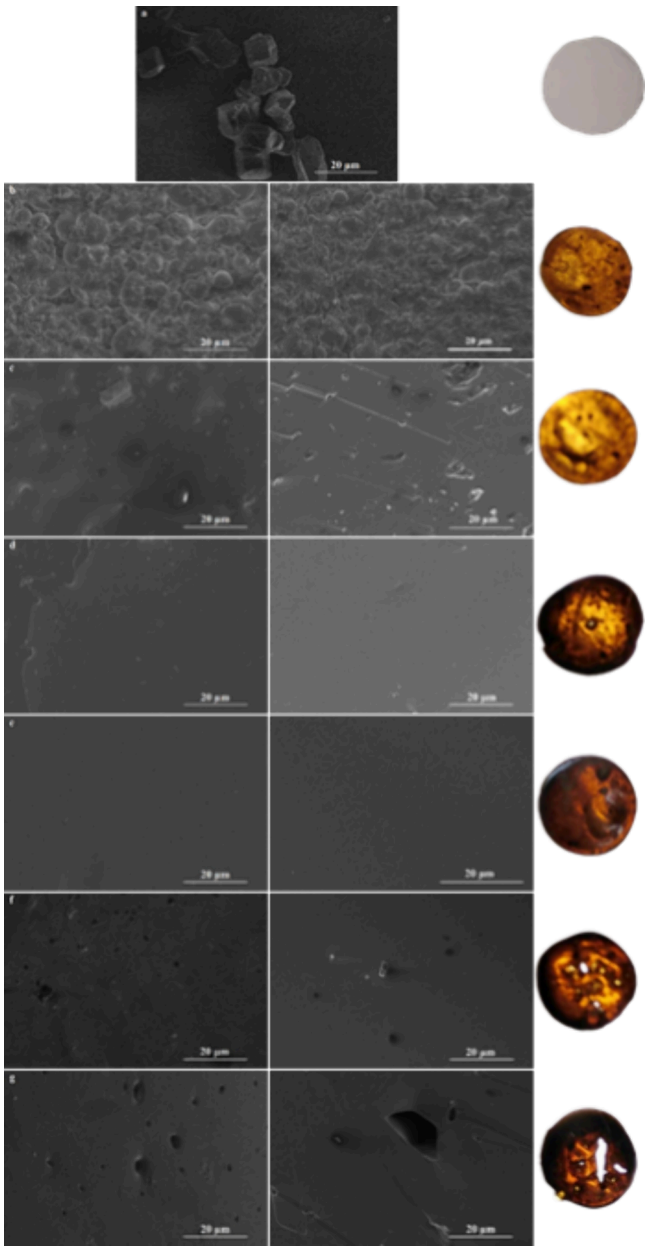

Figure 2. Surface and cross-sectional SEM images, along with photographs of (a) ZIF-62 powder, (b) GMM-400 °C, (c) GMM-415 °C, (d) GMM-430 °C, (e) GMM-445 °C, (f) GMM-460 °C, and (g) GMM-475 °C (for each sample: left, surface SEM image; middle, cross-sectional SEM image; and right, photograph of the GMM).

Figure 3, the GMM-445 (Figure 3e) that was fabricated at 445 °C near the T_m is expected to have the best glass-like properties due to its homogeneous morphology, without exceeding the T_m to cause gradual mesopore and bubble formation.

The crystallinity of the GMMs was assessed with PXRD. The PXRD patterns shown in Figure 4a reveal that the pattern of ZIF-62 matches with the expected phase, while the GMMs are all amorphous and no crystalline phase is found, indicating that the long-range (10s to 100s nm ordering) crystal structure of ZIF-62 has collapsed after the annealing process to produce the GMMs. The two peaks present at 15 and 32 2θ common to the GMM samples are a result of the amorphous halo relating to superposed scattered X-rays as an average of all atomic distances, typical of glasses. As observed in the PXRD patterns, the

https://doi.org/10.1021/acsomega.5c00466
ACS Omega 2025, 10, 7441−7451

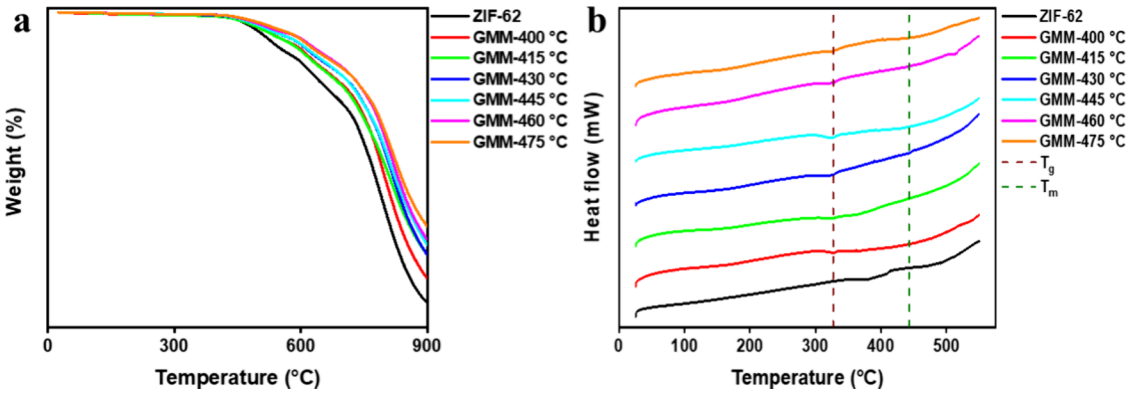

Figure 3. (a) TGA plots and (b) DSC curves of ZIF-62 and fabricated GMMs.

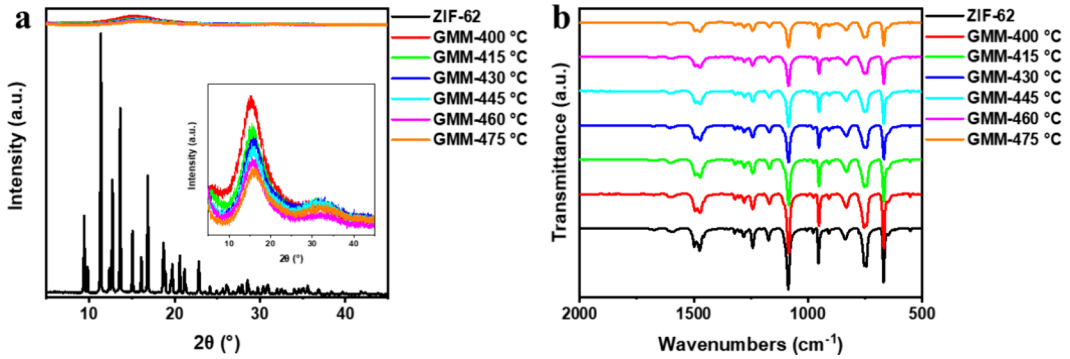

Figure 4. (a) PXRD pattern of ZIF-62 (inset: the PXRD patterns of the GMMs) and (b) FTIR spectra of ZIF-62 and fabricated GMMs.

sharpness and intensity of the diffraction peaks gradually decrease as the sintering temperature increases from 400 to 475 °C. It suggests that the amorphous nature of the GMMs increases as the sintering temperature increases, which is consistent with the structural transformation from a crystalline to a more disordered state. Furthermore, FTIR spectroscopy was employed to study the changes to the chemical bonding and functionality in the structure of the GMMs in comparison to the pristine ZIF-62. Figure 4b shows that the FTIR spectra of ZIF-62 and the GMMs are identical, which suggest that the chemical bonding and functionality of ZIF-62 are preserved within the fabricated GMMs. This shows that the local ordering of ZIF-62 metal-linker bonds are not affected; however, the long-range periodicity, typical of polycrystalline ZIF-62, that would give a narrow and intense peak in a PXRD pattern is affected such that the long-range order within the MOF framework is gradually disturbed as the sintering temperature increases.

To investigate whether the glass transition affects the underlying composition and coordination of ZIF-62, solid-state ^{13}C NMR and XPS were employed. ^{13}C NMR spectra (Figure 5) reveal that the local electronic environments of ^{13}C of pristine ZIF-62 remain largely unaffected under melting at various temperatures. The conjugated C of benzimidazole and imidazole appears at the common heteroaromatic range of 110−150 ppm, with spinning side bands observed ±100 ppm from the main peaks (about 115.2, 122.0 (shoulder), 125.2, 141.7, and 149.2 ppm) with no shifts between all the samples. XPS survey scans and high-resolution scans (Figure 6) and elemental analysis (Table 1) also indicate that the electronic structures remain largely unaffected by glass formation. Although high-resolution scans of the different GMM samples and pristine ZIF-62 indicate a small increase of the binding energy of N 1s from

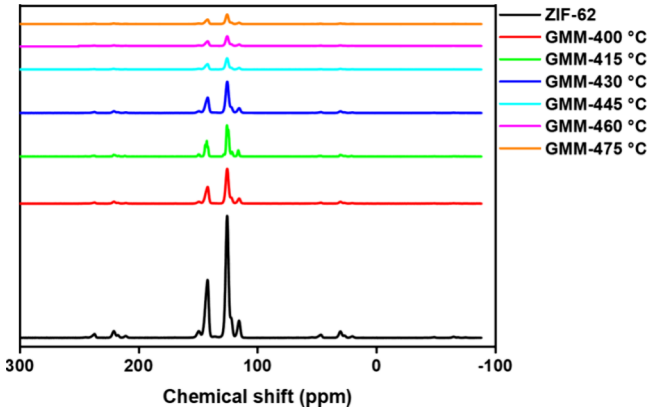

Figure 5. ^{13}C solid-state NMR of ZIF-62 and fabricated GMMs.

403 to 404 eV, the scanning of the C 1s region also shows a broadening of the peak at 289 eV that was deconvoluted to show aromatic C. These observations indicate that limited chemical reactions are taking place during the glass transition and melting processes. The shift in XPS binding energy is attributed to the changing chemical environments around N and C atoms of the linker due to the proximity of the Zn clusters, driven by structural reorganization during glass formation. As the temperature increases during GMM formation, the collapse of the ZIF-62 framework occurs, evidenced by the loss of crystallinity and a reduction in porosity. This collapse reduces the previously fixed interatomic distance between Zn and N in the ordered ZIF-62 structure. Consequently, the Zn clusters are drawn closer to the organic ligands within the GMM, introducing a partial ionic character. This alteration in the chemical environment induces a shift toward higher energy in

https://doi.org/10.1021/acsomega.5c00466
ACS Omega 2025, 10, 7441−7451

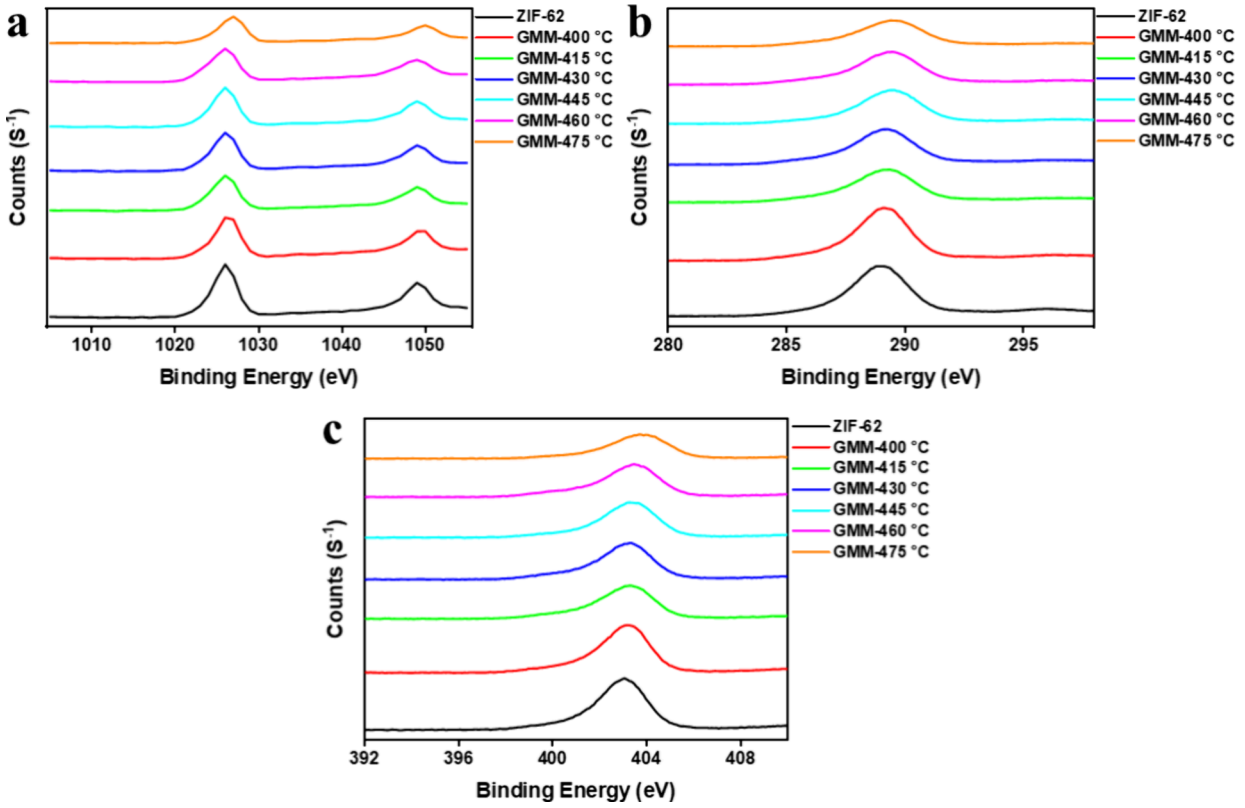

Figure 6. X-ray photoelectron spectra of (a) Zn 2p, (b) C 1s, and (c) N 1s of ZIF-62 and fabricated GMMs.

Table 1. Elemental Analysis of ZIF-62 and Fabricated GMMs Based on XPS Data

MOFs	atomic %		
	Zn	C	N
ZIF-62	8.25	62.19	29.56
GMM-400 °C	7.22	65.29	27.49
GMM-415 °C	8.58	62.41	29.00
GMM-430 °C	8.59	62.05	29.35
GMM-445 °C	8.41	60.94	30.64
GMM-460 °C	8.08	63.23	28.69
GMM-475 °C	8.71	61.40	29.88

the observed N 1s binding energy.[31,63] Moreover, the broadening of the C 1s peak at 289 eV may suggest minor changes in the local electronic density surrounding aromatic carbon atoms, indicating slight modifications in the distribution of electronic density.[56]

The collapse of the ZIF-62 crystal structure within the GMMs impacts their gas adsorption property. The pore structure analysis of the GMMs was performed through low-pressure N_2 and CO_2 gas adsorption measurements. Figure 7a shows the N_2 gas sorption isotherm of ZIF-62 having a monotonic increase for N_2 adsorbed at low relative pressure, which reaches saturation at higher pressures in a typical type I fashion of microporous materials. However, the GMMs do not show N_2 adsorption, suggesting that the porous structure of ZIF-62 has collapsed and is not permeable to N_2. Interestingly, GMM adsorbed CO_2 as indicated by the CO_2 isotherm shown in Figure 7b, as it is smaller than N_2 (3.30 vs 3.65 Å).

However, the loss of the pore structure is also supported by the lower CO_2 adsorption capacities of the GMMs compared to

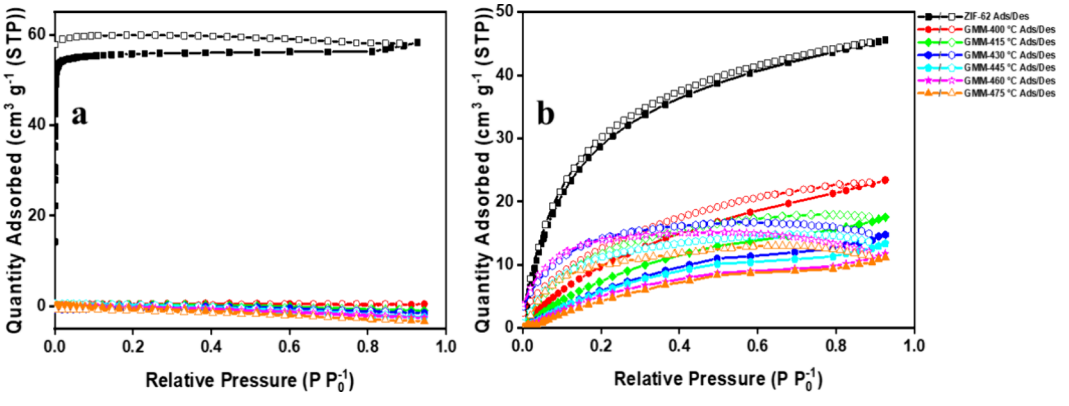

Figure 7. (a) N_2 gas sorption isotherms and (b) CO_2 gas sorption isotherms of ZIF-62 and fabricated GMMs.

https://doi.org/10.1021/acsomega.5c00466
ACS Omega 2025, 10, 7441−7451

those of pristine ZIF-62. From Table 2, the Brunauer–Emmett–Teller surface area (S_{BET}) calculated from N_2

Table 2. BET Surface Area Values for ZIF-62 and GMMs Based on N_2 and CO_2 Adsorption

sample	N_2BET surface area ($m^2\ g^{-1}$)	CO_2BET surface area ($m^2\ g^{-1}$)
ZIF-62	58.8287	148.601
GMM-400 °C	1.9921	66.282
GMM-415 °C	1.4168	53.13
GMM-430 °C	0.6263	47.713
GMM-445 °C	0.0905	44.275
GMM-460 °C	0.0194	39.329
GMM-475 °C	---	30.551

adsorption for ZIF-62 is 58.8 $m^2\ g^{-1}$, which is significantly higher than those for the GMMs (e.g., S_{BET} of GMM-400 is 1.99 $m^2\ g^{-1}$). Also, the S_{BET} of GMMs obtained from CO_2 adsorption is lower than that for the pristine ZIF-62. The S_{BET} decreased as the fabrication temperature of GMM increased.

The pore size distributions calculated from the N_2 and CO_2 adsorption isotherms with DFT show a significant reduction in surface relating to typical micropores of ZIF-62, with pores in the larger range of 10–20 Å for N_2 (Figure 8a). However, for CO_2 derived pore size distributions, micropores retain their positions but significantly reduce in intensity (Figure 8b). The retention of pores between 1 and 10 Å is essential for the sieving of target gases, where the pore size is within the range for sieving H_2 from N_2 or CH_4, for example.

The density of GMMs was studied with He pycnometry using He gas under 2 bar. As revealed in Figure 9, pristine ZIF-62 has the lowest density due to the presence of pore volumes. As the material is heated to 400 °C, the pore structure and the free volume collapse, leading to the formation of highly dense GMM-400. At increased temperature, there is gradual removal of organic component of GMMs since the fabrication occurred under a vacuum, causing a sudden drop in density from 1.62 g cm^{-3} for GMM-400 to 1.56 g cm^{-3} for GMM-415. A slow reduction in GMM density was further observed from 430 to 460 °C. GMM-475 has the least density of the GMMs, which is indicative of the loss of more organic components at elevated temperatures.

Concomitant to N_2 and CO_2 adsorption isotherms and calculated pore size distributions, PALS was utilized to get further insight into the pore architecture of GMMs, where the

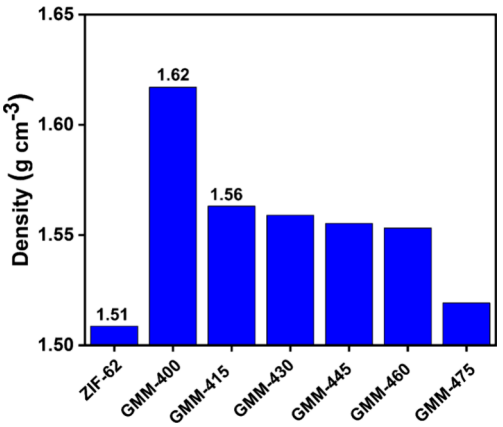

Figure 9. Densities of ZIF-62 and fabricated GMMs based on He pycnometry.

lifetime, τ, is related to the pore size and the intensity, I, is related to the abundance of pores. Based on the PALS results, the most suitable fit was with three components for ZIF-62 and four components for the GMMs, which correspond to a single (τ_3, I_3) and bimodal (τ_3, I_3 and τ_4, I_4) pore distribution, respectively. As shown in Figure 10a,b, when the temperature was increased to 445 °C, the GMMs demonstrated shorter lifetimes, whereas when the temperature was further increased, the GMMs displayed longer lifetimes. Similar observations were made for both small and large pores in the GMMs (Figure 10c). Moreover, as presented in Figure 10a,b, as the temperature increases up to 445 °C, the intensity of small pores (Intensity3) increases and then decreases with further temperature increases, whereas the GMMs showed the opposite pattern for the intensity of large pores (Intensity4). Overall, these results demonstrate that the initial temperature increments lead to more smaller pores and fewer larger pores because a suitable glass with a greater molecular sieving behavior is formed. However, as the temperature further increased, the smaller pores were reduced, while the larger pores were increased due to the decomposition of the structure.

Gas Separation Performance. In Figure 11a, single gas permeation is represented as a function of molecular kinetic diameter in separation by GMM-445. Permeation was shown to be negatively correlated to the kinetic diameters of permeant molecules and positively correlated with framework flexibility. The gas permeation measured for He, H_2, CO_2, N_2, and CH_4

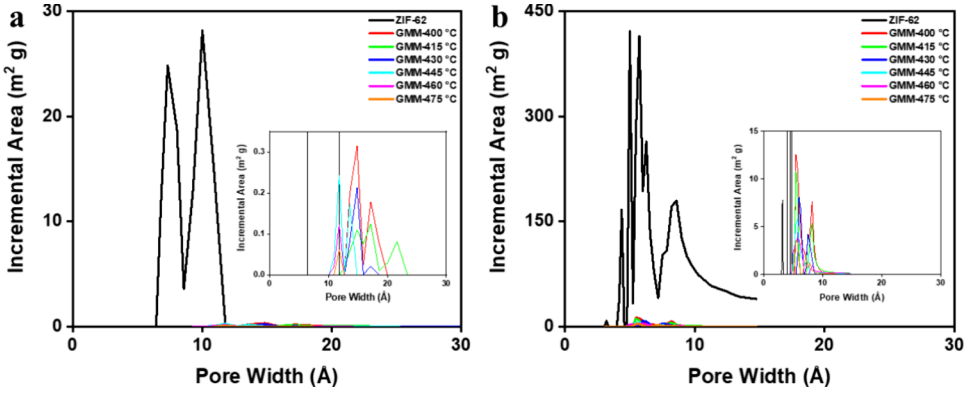

Figure 8. (a) Pore size distribution using N_2 gas sorption isotherms and (b) pore size distribution using CO_2 gas sorption isotherms of ZIF-62 and fabricated GMMs.

https://doi.org/10.1021/acsomega.5c00466
ACS Omega 2025, 10, 7441–7451

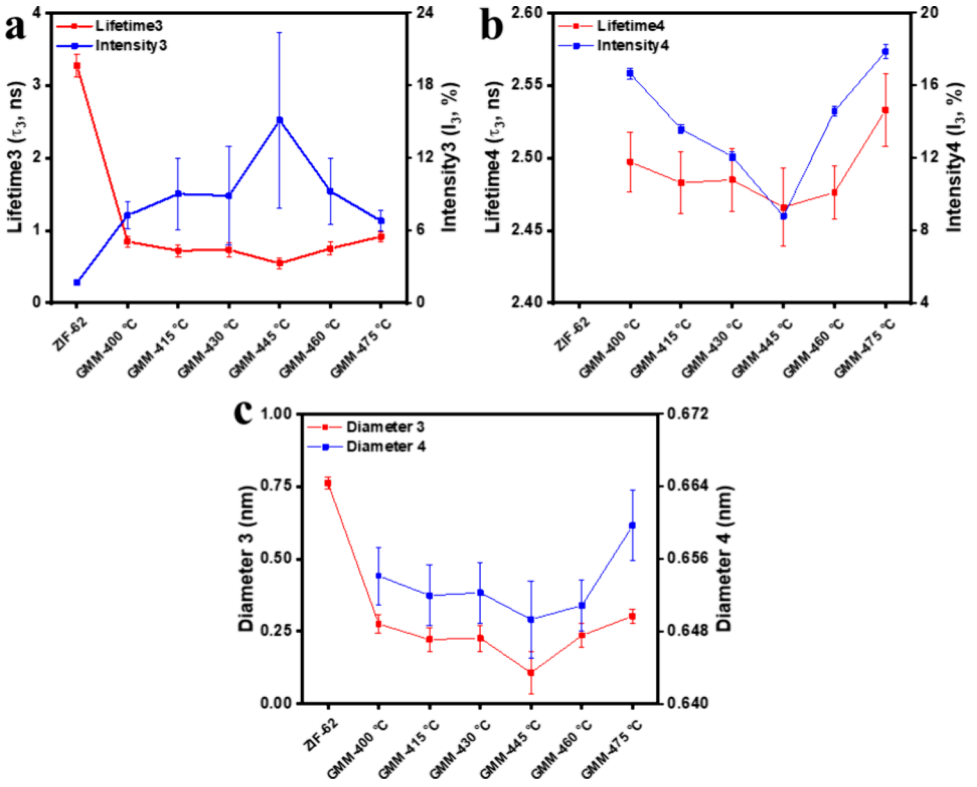

Figure 10. PALS obtained lifetimes and intensities of (a) third and (b) fourth curve fits in the Tao−Eldrup model to obtain (c) pore diameters of ZIF-62 and fabricated GMMs.

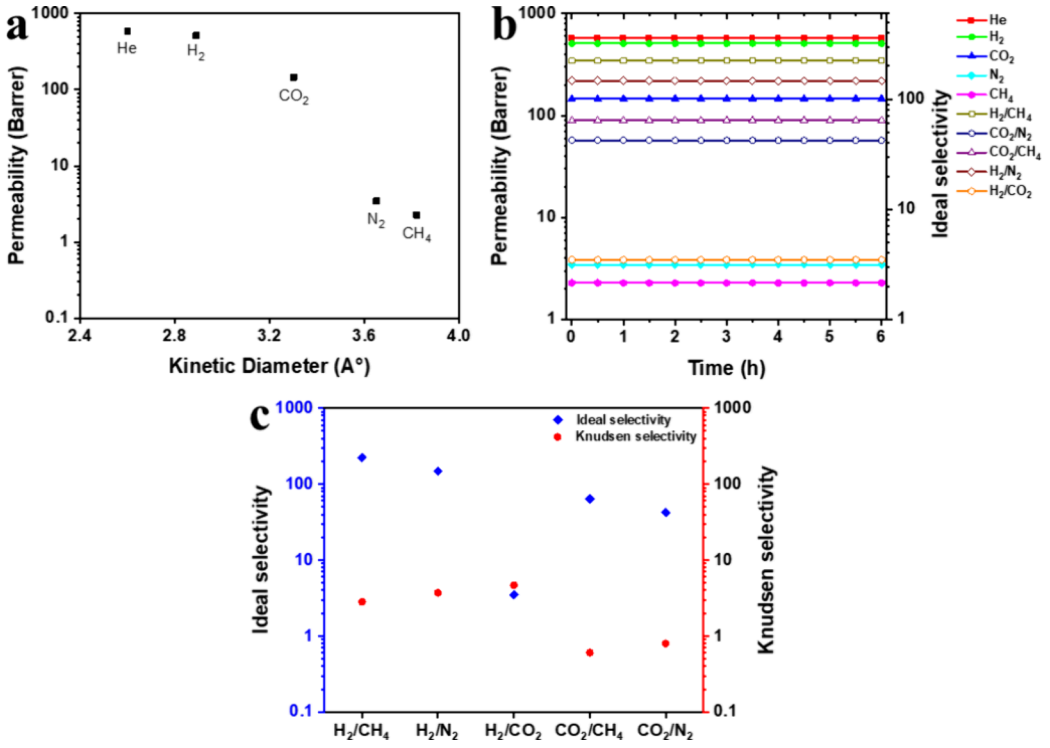

Figure 11. GMM (a) average gas permeability as a function of kinetic diameter; (b) gas permeability and ideal selectivity as a function of time; and (c) ideal and Knudsen selectivities of H_2/CH_4, H_2/N_2, H_2/CO_2, CO_2/CH_4, and CO_2/N_2 gas pairs at 4 bar and 25 °C.

gases at 4 bar and 25 °C were 576.37, 509.23, 146.07, 3.45, and 2.28 barrer, respectively. In fact, the GMM allowed molecules larger than the aperture size to pass through with regard to the flexibility of the framework.[64−66] Besides, the remarkable difference between CO_2, and N_2 permeation values indicates that the GMM has an average accessible pore diameter between the molecular kinetic diameters for CO_2 and N_2 (Figure 12). On the other hand, the GMMs' stability was evaluated by

https://doi.org/10.1021/acsomega.5c00466
ACS Omega 2025, 10, 7441−7451

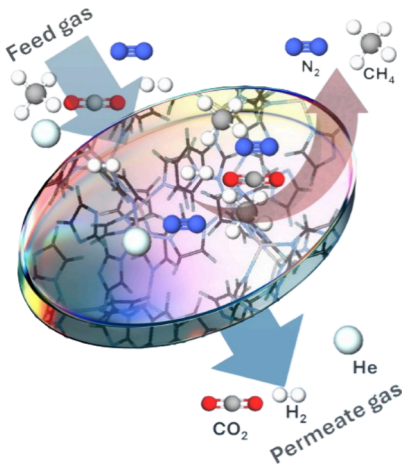

Figure 12. Permeation variations of the GMM across different gases.

monitoring the gas permeability and ideal selectivity for He, H_2, CO_2, N_2, and CH_4 gases and H_2/CH_4, H_2/N_2, H_2/CO_2, CO_2/CH_4, and CO_2/N_2 gas pairs at 4 bar and 25 °C over a 6 h (Figure 11b). The results indicate consistent permeability and selectivity values for all gases and gas pairs, respectively, demonstrating the membrane's structural and functional stability under test conditions. This stability suggests the GMM's potential for long-term application in industrial gas separation processes, as it maintains both its permeability and selectivity without a decline over time. Moreover, the ideal selectivity values, which is defined as the ratio of fast to slow gas permeability, for H_2/CH_4, CO_2/N_2, CO_2/CH_4, H_2/N_2, and H_2/CO_2 gas pairs at 4 bar and 25 °C were 223.47, 42.37, 64.10, 147.71, and 3.49, respectively (Figure 11c). The ideal selectivity for most of the gas pairs (H_2/CH_4, CO_2/N_2, CO_2/CH_4, and H_2/N_2) not only greatly exceeded the corresponding Knudsen selectivity (2.82, 0.80, 0.60, and 3.73, respectively) derived by the inverse of the square root of the molecular masses but also surpassed the performance of previously reported ZIF-62 supported glass membranes (H_2/CH_4 = 50).[42] This significant enhancement highlights the importance of systematic thermal optimization and self-supporting structures in improving the molecular sieving performance. The Knudsen selectivity is commonly employed to benchmark a membrane's performance, as molecular sieving will occur if the membrane's selectivity is above that value; otherwise, it will contain pinholes or mesopores. Due to GMM's limited affinity for the measured gases, the high ideal selectivity is highly dependent on the molecular sieving mechanism.[42,43] It was observed, however, that the H_2/CO_2 pair exhibited close to ideal selectivity and Knudsen selectivity; this is consistent with the previously speculated GMM having an average pore diameter that lies between the molecular kinetic diameters of the two atoms, CO_2 and N_2. It is evident by the ideal selectivities that this GMM membrane exhibited a marked improvement over Knudsen's selectivities and that the intercrystal and grain boundary defects have been overcome to a great extent. Therefore, the high ideal selectivities along with suitable gas permeations suggesting the molecular sieving potential of ZIF-62 were highly accomplished in GMM formation.

As a means of comparing the gas separation performance of the GMM, the positions of its data points in the selectivity-permeability plot (termed the Robeson diagram) were considered. The target for research materials is to pass over the upper bound of the Robeson diagram that initially emerged in 1991 (Robeson's upper bound 1991), was significantly revised in 2008 (Robeson's upper bound 2008), and was most recently reviewed in 2015 (Robeson's upper bound 2015). Therefore, permeation results for all the pair gases at 25 °C and 4 bar pressure were presented and plotted in the Robeson diagrams in Tables S3−S7 and Figures S1−S5. The position of the data point obtained from the fabricated GMM in Figure 13

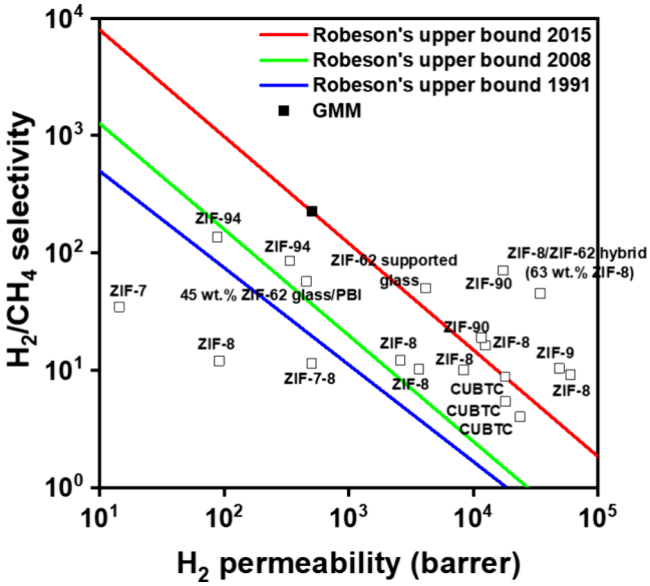

Figure 13. Comparison of the H_2/CH_4 separation performances of the GMM with literature data.

for H_2/CH_4 separation passes over the Robeson upper bounds, which is an excellent gas separation performance result. In addition, it was also found that the GMM separated gases with smaller and equal kinetic diameters of CO_2 better than gases with larger and equal kinetic diameters of N_2. As the data point positions exceeded Robeson's upper bound 2015, the gas separation performance of GMMs was found to be exceptional. This achievement highlights their capability to exceed established benchmarks in the membrane gas separation field. Moreover, the gas separation performance of some MOF-based membranes reported in the literature has been compared with the GMM gas separation performance (Tables S3−S7 and Figures S1−S5).

As can be seen, polycrystalline MOF membranes exhibit high separation performance, as previously mentioned; however, they are often limited by interfacial voids and grain boundary defects. To reduce these limitations, strategies such as crystal orientation adjustment and defect elimination are implemented to enhance performance.[55,67,68] In contrast, the absence of intercrystal and grain boundary defects in glassy MOFs results in their inherent high gas separation performance. Moreover, gas separation performance can be further improved by incorporating various metal nodes (e.g., Co and Zn)[58] or by fabricating composites with other materials such as ZIF-7, ZIF-8, CA, and PIM through modifying porosity and affinities with target gases.[21,36,59,60] Additionally, gas separation properties are highly influenced by the synthesis approach; for example, controlling membrane thickness by cathodic deposition followed by melt quenching can significantly enhance separation performance.[69] Based on the results, the data point positions of the fabricated GMM were higher than those of most of the other MOF-based membranes.

https://doi.org/10.1021/acsomega.5c00466
ACS Omega 2025, 10, 7441−7451

Furthermore, it was found that the H_2/CO_2 separation data position was not as good as other gas pairs when compared with other MOF-based membranes. This occurs as a result of GMM having an average accessible pore diameter that is between the molecular kinetic diameters of CO_2 and N_2. Accordingly, GMM can be good candidates for gas separation.

CONCLUSIONS

The self-supporting GMMs are a suitable solution for gas separation due to their significant porosity of polycrystalline MOFs, ease of processing, and potential to eliminate grain boundaries. This study systematically examines the effect of thermal treatment temperatures, optimizing the vitrification process to enhance the gas separation performance. The GMM fabricated from ZIF-62 demonstrates exceptional separation capabilities due to its remarkable improvement in molecular sieving through vitrification due to the high glass-forming ability and lack of intermediate recrystallization, resulting in remarkable improvements in the gas separation performance compared to previous reports. The GMM at 4 bar and 25 °C exhibited He, H_2, CO_2, N_2, and CH_4 gas permeations of 576.37, 509.23, 146.07, 3.45, and 2.28 barrer, respectively. It was shown that permeation results were negatively correlated with the kinetic diameter of the permeant molecules and positively correlated with the flexibility of the framework. The ideal selectivities of H_2/CH_4, CO_2/N_2, CO_2/CH_4, H_2/N_2, and H_2/CO_2 gas pairs were 223.47, 42.37, 64.10, 147.71, and 3.49, respectively. Molecular sieving is thought to be responsible for the high ideal selectivities. The GMM membranes exhibited a marked improvement over Knudsen's selectivities, clearly showing that intercrystal and grain boundary defects have been overcome. This suggests that the molecular sieving potential of ZIF-62 was highly accomplished during GMM formation, as evidenced by the appropriate gas permeations and high ideal selectivities. Besides, since the data point positions exceeded Robeson's upper bound, the GMM can be considered high-performance gas separation membranes. This study indicated that GMM has the potential to develop next-generation molecular sieve membranes for gas separation toward ultimate gas separation.

ASSOCIATED CONTENT

Supporting Information

The Supporting Information is available free of charge at https://pubs.acs.org/doi/10.1021/acsomega.5c00466.

Chemicals; nanoparticle synthesis; GMM preparation; and characterization methodologies including SEM, TGA, DSC, PXRD, FTIR, ^{13}C NMR, XPS, low-pressure gas sorption, He pycnometry, and PALS, as well as gas permeation measurement (PDF)

AUTHOR INFORMATION

Corresponding Authors

Stefan J.D. Smith − *Department of Chemical and Biological Engineering, Monash University, Clayton, Victoria 3800, Australia; CSIRO Manufacturing, Clayton South, Victoria 3169, Australia;* orcid.org/0000-0001-7465-0565; Email: stefan.smith@monash.edu

Xavier Mulet − *CSIRO Manufacturing, Clayton South, Victoria 3169, Australia; Applied Chemistry and Environmental Science, School of Science, RMIT University, Melbourne, Victoria 3000, Australia*; Email: xavier.mulet2@rmit.edu.au

Matthew R. Hill − *CSIRO Manufacturing, Clayton South, Victoria 3169, Australia; Department of Materials Science and Engineering, Monash University, Clayton, Victoria 3800, Australia;* orcid.org/0000-0001-8897-0324; Email: matthew.hill@monash.edu, matthew.hill@csiro.au

Authors

Hamidreza Mahdavi − *Department of Chemical and Biological Engineering, Monash University, Clayton, Victoria 3800, Australia; CSIRO Manufacturing, Clayton South, Victoria 3169, Australia;* orcid.org/0000-0001-8175-4303

Joseph F. Olorunyomi − *CSIRO Manufacturing, Clayton South, Victoria 3169, Australia; Applied Chemistry and Environmental Science, School of Science, RMIT University, Melbourne, Victoria 3000, Australia*

Nathan T. Eden − *Department of Chemical and Biological Engineering, Monash University, Clayton, Victoria 3800, Australia;* orcid.org/0000-0002-1456-1381

Cara M. Doherty − *CSIRO Manufacturing, Clayton South, Victoria 3169, Australia*

Durga Acharya − *CSIRO Manufacturing, Clayton South, Victoria 3169, Australia;* orcid.org/0000-0001-6900-6230

Complete contact information is available at: https://pubs.acs.org/10.1021/acsomega.5c00466

Author Contributions

H.M. led the project administration, conceptual and experimental design, analysis, interpretation of results, and writing the draft. J.F.O contributed to the synthesis, analysis, interpretation of results and writing the draft. N.T.E contributed to the analysis, interpretation of results, and writing the draft. C.M.D. and D.A. led the experimental design and data curation of PALS experiments presented. S.J.D.S., X.M., and M.R.H. contributed to the project administration, conceptual and experimental design, analysis, and interpretation of results.

Notes

The authors declare no competing financial interest.

ACKNOWLEDGMENTS

The authors acknowledge the use of facilities within the Monash X-ray Platform and Monash Centre for Electron Microscopy.

REFERENCES

(1) Ahmadpour, E.; Shamsabadi, A. A.; Behbahani, R. M.; Aghajani, M.; Kargari, A. Study of CO_2 separation with PVC/Pebax composite membrane. *J. Nat. Gas Sci. Eng.* **2014**, *21*, 518−523.

(2) Car, A.; Stropnik, C.; Yave, W.; Peinemann, K.-V. Pebax®/polyethylene glycol blend thin film composite membranes for CO_2 separation: Performance with mixed gases. *Sep. Purif. Technol.* **2008**, *62*, 110−117.

(3) Sholl, D. S.; Lively, R. P. Seven chemical separations to change the world. *Nature* **2016**, *532*, 435−437.

(4) Ockwig, N. W.; Nenoff, T. M. Membranes for Hydrogen Separation. *Chem. Rev.* **2007**, *107*, 4078−4110.

(5) Li, Y.-S.; Liang, F.-Y.; Bux, H.; Feldhoff, A.; Yang, W.-S.; Caro, J. Molecular Sieve Membrane: Supported Metal−Organic Framework with High Hydrogen Selectivity. *Angew. Chem., Int. Ed.* **2010**, *49*, 548−551.

(6) Pham, T. C. T.; Kim, H. S.; Yoon, K. B. Growth of Uniformly Oriented Silica MFI and BEA Zeolite Films on Substrates. *Science* **2011**, *334*, 1533−1538.

(7) Anson, M.; Marchese, J.; Garis, E.; Ochoa, N.; Pagliero, C. ABS copolymer-activated carbon mixed matrix membranes for CO_2/CH_4 separation. *J. Membr. Sci.* **2004**, *243*, 19−28.
(8) Okabe, K.; Mano, H.; Fujioka, Y. Separation and recovery of carbon dioxide by a membrane flash process. *Int. J. Greenhouse Gas Control* **2008**, *2*, 485−491.
(9) Baker, R. W.*Membrane technology and applications*; John Wiley & Sons: 2012.
(10) Sondhi, R.; Bhave, R.; Jung, G. Applications and benefits of ceramic membranes. *Membr. Technol.* **2003**, *2003*, 5−8.
(11) Nazari, M.; Zadehahmadi, F.; Sadiq, M. M.; Sutton, A. L.; Mahdavi, H.; Hill, M. R. Challenges and solutions to the scale-up of porous materials. *Commun. Mater.* **2024**, *5*, 170.
(12) Batten, S. R.; Champness, N. R.; Chen, X.-M.; Garcia-Martinez, J.; Kitagawa, S.; Öhrström, L.; O'Keeffe, M.; Suh, M. P.; Reedijk, J. Terminology of metal−organic frameworks and coordination polymers (IUPAC Recommendations 2013). *Pure Appl. Chem.* **2013**, *85*, 1715−1724.
(13) Zhou, H.-C. J.; Kitagawa, S. Metal−Organic Frameworks (MOFs). *Chem. Soc. Rev.* **2014**, *43*, 5415−5418.
(14) Mahdavi, H.; Eden, N. T.; Doherty, C. M.; Acharya, D.; Smith, S. J. D.; Mulet, X.; Hill, M. R. Underlying Polar and Nonpolar Modification MOF-Based Factors that Influence Permanent Porosity in Porous Liquids. *ACS Appl. Mater. Interfaces* **2022**, *14*, 23392−23399.
(15) Ma, X.; Kumar, P.; Mittal, N.; Khlyustova, A.; Daoutidis, P.; Mkhoyan, K. A.; Tsapatsis, M. Zeolitic imidazolate framework membranes made by ligand-induced permselectivation. *Science* **2018**, *361*, 1008−1011.
(16) Peng, Y.; Li, Y.; Ban, Y.; Jin, H.; Jiao, W.; Liu, X.; Yang, W. Metal-organic framework nanosheets as building blocks for molecular sieving membranes. *Science* **2014**, *346*, 1356−1359.
(17) Shen, K.; Zhang, L.; Chen, X.; Liu, L.; Zhang, D.; Han, Y.; Chen, J.; Long, J.; Luque, R.; Li, Y.; Chen, B. Ordered macro-microporous metal-organic framework single crystals. *Science* **2018**, *359*, 206−210.
(18) Qiao, Z.; Zhao, S.; Wang, J.; Wang, S.; Wang, Z.; Guiver, M. D. A Highly Permeable Aligned Montmorillonite Mixed-Matrix Membrane for CO_2 Separation. *Angew. Chem., Int. Ed.* **2016**, *55*, 9321−9325.
(19) Mahdavi, H.; Zhang, H.; Macreadie, L. K.; Doherty, C. M.; Acharya, D.; Smith, S. J. D.; Mulet, X.; Hill, M. R. Underlying solvent-based factors that influence permanent porosity in porous liquids. *Nano Res.* **2022**, *15*, 3533−3538.
(20) Yang, Z.; Belmabkhout, Y.; McHugh, L. N.; Ao, D.; Sun, Y.; Li, S.; Qiao, Z.; Bennett, T. D.; Guiver, M. D.; Zhong, C. ZIF-62 glass foam self-supported membranes to address CH_4/N_2 separations. *Nat. Mater.* **2023**, *22*, 888−894.
(21) Feng, Y.; Yan, W.; Kang, Z.; Zou, X.; Fan, W.; Jiang, Y.; Fan, L.; Wang, R.; Sun, D. Thermal treatment optimization of porous MOF glass and polymer for improving gas permeability and selectivity of mixed matrix membranes. *Chem. Eng. J.* **2023**, *465*, No. 142873.
(22) Oyama, S. T.; Yamada, M.; Sugawara, T.; Takagaki, A.; Kikuchi, R. Review on Mechanisms of Gas Permeation through Inorganic Membranes. *J. Jpn. Pet. Inst.* **2011**, *54*, 298−309.
(23) Pera-Titus, M. Porous Inorganic Membranes for CO_2 Capture: Present and Prospects. *Chem. Rev.* **2014**, *114*, 1413−1492.
(24) Yan, J.; Sun, Y.; Ji, T.; Liu, L.; Zhang, M.; Liu, Y. Cooperative defect tailoring: A promising protocol for exceeding performance limits of state-of-the-art MOF membranes. *J. Membr. Sci.* **2021**, *635*, No. 119515.
(25) Park, S.; Cho, K. Y.; Jeong, H.-K. Enhancing the propylene/propane separation performances of ZIF-8 membranes by post-synthetic surface polymerization. *J. Mater. Chem. A* **2022**, *10*, 1940−1947.
(26) Sheng, L.; Wang, C.; Yang, F.; Xiang, L.; Huang, X.; Yu, J.; Zhang, L.; Pan, Y.; Li, Y. Enhanced C_3H_6/C_3H_8 separation performance on MOF membranes through blocking defects and hindering framework flexibility by silicone rubber coating. *Chem. Commun.* **2017**, *53*, 7760−7763.
(27) Nomura, M.; Yamaguchi, T.; Nakao, S.-i. Transport phenomena through intercrystalline and intracrystalline pathways of silicalite zeolite membranes. *J. Membr. Sci.* **2001**, *187*, 203−212.
(28) Gaillac, R.; Pullumbi, P.; Beyer, K. A.; Chapman, K. W.; Keen, D. A.; Bennett, T. D.; Coudert, F.-X. Liquid metal−organic frameworks. *Nat. Mater.* **2017**, *16*, 1149−1154.
(29) Tuffnell, J. M.; Ashling, C. W.; Hou, J.; Li, S.; Longley, L.; Ríos Gómez, M. L.; Bennett, T. D. Novel metal−organic framework materials: blends, liquids, glasses and crystal−glass composites. *Chem. Commun.* **2019**, *55*, 8705−8715.
(30) Bennett, T. D.; Horike, S. Liquid, glass and amorphous solid states of coordination polymers and metal−organic frameworks. *Nat. Rev. Mater.* **2018**, *3*, 431−440.
(31) Ma, N.; Horike, S. Metal−Organic Network-Forming Glasses. *Chem. Rev.* **2022**, *122*, 4163−4203.
(32) Li, S.; Limbach, R.; Longley, L.; Shirzadi, A. A.; Walmsley, J. C.; Johnstone, D. N.; Midgley, P. A.; Wondraczek, L.; Bennett, T. D. Mechanical Properties and Processing Techniques of Bulk Metal−Organic Framework Glasses. *J. Am. Chem. Soc.* **2019**, *141*, 1027−1034.
(33) Madsen, R. S. K.; Qiao, A.; Sen, J.; Hung, I.; Chen, K.; Gan, Z.; Sen, S.; Yue, Y. Ultrahigh-field 67Zn NMR reveals short-range disorder in zeolitic imidazolate framework glasses. *Science* **2020**, *367*, 1473−1476.
(34) Yu, S.; Li, C.; Zhao, S.; Chai, M.; Hou, J.; Lin, R. Recent advances in the interfacial engineering of MOF-based mixed matrix membranes for gas separation. *Nanoscale* **2024**, *16*, 7716−7733.
(35) Ao, D.; Yang, Z.; Qiao, Z.; Sun, Y.; Zhang, Z.; Guiver, M. D.; Zhong, C. Metal−Organic Framework Crystal−Glass Composite Membranes with Preferential Permeation of Ethane. *Angew. Chem.* **2023**, *135*, No. e202304535.
(36) Li, D.; Yang, Z.; Yang, L.; Ma, C.; Ye, M.; Sun, Y.; Qiao, Z.; Chen, A. Self-supported flux melted glass membranes fabricated by melt quenching for gas separation. *J. Membr. Sci.* **2024**, *695*, No. 122492.
(37) Zhou, C.; Longley, L.; Krajnc, A.; Smales, G. J.; Qiao, A.; Erucar, I.; Doherty, C. M.; Thornton, A. W.; Hill, A. J.; Ashling, C. W.; Qazvini, O. T.; Lee, S. J.; Chater, P. A.; Terrill, N. J.; Smith, A. J.; Yue, Y.; Mali, G.; Keen, D. A.; Telfer, S. G.; Bennett, T. D. Metal-organic framework glasses with permanent accessible porosity. *Nat. Commun.* **2018**, *9*, 5042.
(38) Tao, H.; Bennett, T. D.; Yue, Y. Melt-Quenched Hybrid Glasses from Metal−Organic Frameworks. *Adv. Mater.* **2017**, *29*, No. 1601705.
(39) Longley, L.; Collins, S. M.; Li, S.; Smales, G. J.; Erucar, I.; Qiao, A.; Hou, J.; Doherty, C. M.; Thornton, A. W.; Hill, A. J.; Yu, X.; Terrill, N. J.; Smith, A. J.; Cohen, S. M.; Midgley, P. A.; Keen, D. A.; Telfer, S. G.; Bennett, T. D. Flux melting of metal−organic frameworks. *Chem. Sci.* **2019**, *10*, 3592−3601.
(40) Hou, J.; Ashling, C. W.; Collins, S. M.; Krajnc, A.; Zhou, C.; Longley, L.; Johnstone, D. N.; Chater, P. A.; Li, S.; Coulet, M.-V.; Llewellyn, P. L.; Coudert, F.-X.; Keen, D. A.; Midgley, P. A.; Mali, G.; Chen, V.; Bennett, T. D. Metal-organic framework crystal-glass composites. *Nat. Commun.* **2019**, *10*, 2580.
(41) Li, S.; Yu, S.; Collins, S. M.; Johnstone, D. N.; Ashling, C. W.; Sapnik, A. F.; Chater, P. A.; Keeble, D. S.; McHugh, L. N.; Midgley, P. A.; Keen, D. A.; Bennett, T. D. A new route to porous metal−organic framework crystal−glass composites. *Chem. Sci.* **2020**, *11*, 9910−9918.
(42) Wang, Y.; Jin, H.; Ma, Q.; Mo, K.; Mao, H.; Feldhoff, A.; Cao, X.; Li, Y.; Pan, F.; Jiang, Z. A MOF Glass Membrane for Gas Separation. *Angew. Chem., Int. Ed.* **2020**, *59*, 4365−4369.
(43) Xia, H.; Jin, H.; Zhang, Y.; Song, H.; Hu, J.; Huang, Y.; Li, Y. A long-lasting TIF-4 MOF glass membrane for selective CO_2 separation. *J. Membr. Sci.* **2022**, *655*, No. 120611.
(44) Sun, Y.; Liu, Y. Design of metal-organic framework membranes towards ultimate gas separation. *Green Chem. Eng.* **2021**, *2*, 14−16.
(45) Ma, C.; Li, N.; Li, D.; Gu, Z.; Qiao, Z.; Zhong, C. A self-supported a_gZIF-UC-4 glass membrane for gas separation. *J. Membr. Sci.* **2023**, *683*, No. 121873.
(46) Qiao, A.; Bennett, T. D.; Tao, H.; Krajnc, A.; Mali, G.; Doherty, C. M.; Thornton, A. W.; Mauro, J. C.; Greaves, G. N.; Yue, Y. A metal-

https://doi.org/10.1021/acsomega.5c00466
ACS Omega 2025, 10, 7441−7451

organic framework with ultrahigh glass-forming ability. *Sci. Adv.* **2018**, *4*, No. eaao6827.
(47) Xiong, M.; Zhao, X.; Yin, G.; Ching, W.-Y.; Li, N. Unraveling the effects of linker substitution on structural, electronic and optical properties of amorphous zeolitic imidazolate frameworks-62 (a-ZIF-62) glasses: a DFT study. *RSC Adv.* **2020**, *10*, 14013−14024.
(48) Fonseca, J.; Gong, T.; Jiao, L.; Jiang, H.-L. Metal−organic frameworks (MOFs) beyond crystallinity: amorphous MOFs, MOF liquids and MOF glasses. *J. Mater. Chem. A* **2021**, *9*, 10562−10611.
(49) Huang, L.; Xing, Z.; Zhuang, X.; Wei, J.; Ma, Y.; Wang, B.; Jiang, X.; He, X.; Deng, L.; Dai, Z. Polymeric membranes and their derivatives for H_2/CH_4 separation: State of the art. *Sep. Purif. Technol.* **2022**, *297*, No. 121504.
(50) Liu, Y.; Zhou, C.; Chen, L.; Du, J.; Li, Q.; Lu, C.; Tan, L.; Huang, X.; Liu, J.; Dong, L. Self-standing membranes for separation: Achievements and opportunities. *Adv. Colloid Interface Sci.* **2024**, *332*, No. 103269.
(51) To, T.; Sørensen, S. S.; Stepniewska, M.; Qiao, A.; Jensen, L. R.; Bauchy, M.; Yue, Y.; Smedskjaer, M. M. Fracture toughness of a metal−organic framework glass. *Nat. Commun.* **2020**, *11*, 2593.
(52) Yan, S.; Bennett, T. D.; Feng, W.; Zhu, Z.; Yang, D.; Zhong, Z.; Qin, Q. H. Brittle-to-ductile transition and theoretical strength in a metal−organic framework glass. *Nanoscale* **2023**, *15*, 8235−8244.
(53) Widmer, R. N.; Bumstead, A. M.; Jain, M.; Bennett, T. D.; Michler, J. Plasticity of metal−organic framework glasses. *J. Am. Chem. Soc.* **2021**, *143*, 20717−20724.
(54) Zhang, Y.; Cui, H.; Hu, X.; Wang, S.; Zhu, X.; Li, H.; Song, X.; Wei, N.; Li, J. The non-crystalline metal-organic framework for corrosion inhibitor behavior in sodium chloride solution. *Mater. Today Commun.* **2022**, *33*, No. 104519.
(55) Zhao, Z.; Ding, L.; Mundstock, A.; Stölting, O.; Polarz, S.; Wang, H.; Feldhoff, A. Preparation of ZIF-62 polycrystalline and glass membranes for helium separation. *J. Membr. Sci.* **2024**, *700*, No. 122677.
(56) Ye, M.; Ao, D.; Sun, Y.; Gu, Z.; Yang, Z.; Qiao, Z. Preparation and Performance of a Novel Self-supported ZIF Glass Membrane for Gas Separation. *J. Chin. Ceram. Soc.* **2024**, *52*, 2545−2552.
(57) Li, Z.; Wang, Y.; Zhang, J.; Cheng, S.; Sun, Y. A Short Review of Advances in MOF Glass Membranes for Gas Adsorption and Separation. *Membranes* **2024**, *14*, 99.
(58) Zhong, L.; Du, Z.; Guo, S.; Ren, X.; Qiao, A.; Tao, H. Gas separation in bimetallic Zn/Co-ZIF-62 glass membrane. *Funct. Mater. Lett.* **2024**, *17*, 2451036−2451046.
(59) Mubashir, M.; Dumée, L. F.; Fong, Y. Y.; Jusoh, N.; Lukose, J.; Chai, W. S.; Show, P. L. Cellulose acetate-based membranes by interfacial engineering and integration of ZIF-62 glass nanoparticles for CO_2 separation. *J. Hazard. Mater.* **2021**, *415*, No. 125639.
(60) Zhang, Y.; Wang, Y.; Xia, H.; Gao, P.; Cao, Y.; Jin, H.; Li, Y. A hybrid ZIF-8/ZIF-62 glass membrane for gas separation. *Chem. Commun.* **2022**, *58*, 9548−9551.
(61) Chen, X.; Song, S.; Wang, L.; Zhang, X.; Fu, D.; Zhang, G. Ultrathin Metal-Organic Framework Membranes Used for Industrial Separation. *Earth Environ. Sci.* **2018**, *170*, No. 052040.
(62) Kang, D.-Y.; Hung, H.-L.; Tsai, H.-Y.; Lai, J.-Y.; Hung, T.-H.Metal-organic framework membranes for gas separation and pervaporation. In *60 Years of the Loeb-Sourirajan Membrane*; Elsevier: 2022, 215−238.
(63) Calahoo, C.; Wondraczek, L. Ionic glasses: Structure, properties and classification. *J. Non-Cryst. Solids X* **2020**, *8*, No. 100054.
(64) Hwang, S.; Semino, R.; Seoane, B.; Zahan, M.; Chmelik, C.; Valiullin, R.; Bertmer, M.; Haase, J.; Kapteijn, F.; Gascon, J.; Maurin, G.; Kärger, J. Revealing the Transient Concentration of CO_2 in a Mixed-Matrix Membrane by IR Microimaging and Molecular Modeling. *Angew. Chem., Int. Ed.* **2018**, *57*, 5156−5160.
(65) Brown, A. J.; Brunelli, N. A.; Eum, K.; Rashidi, F.; Johnson, J. R.; Koros, W. J.; Jones, C. W.; Nair, S. Interfacial microfluidic processing of metal-organic framework hollow fiber membranes. *Science* **2014**, *345*, 72−75.
(66) Chen, C.; Ozcan, A.; Yazaydin, A. O.; Ladewig, B. P. Gas permeation through single-crystal ZIF-8 membranes. *J. Membr. Sci.* **2019**, *575*, 209−216.
(67) Dorosti, F.; Ge, L.; Wang, H.; Zhu, Z. A path forward: Understanding and mitigating defects in polycrystalline membranes. *Prog. Mater. Sci.* **2023**, *137*, No. 101123.
(68) Lian, H.; Bao, B.; Chen, J.; Yang, W.; Yang, Y.; Hou, R.; Ju, S.; Pan, Y. Manipulation strategies for improving gas separation performance on metal-organic frameworks membranes. *Results in Eng.* **2022**, *15*, No. 100609.
(69) Xie, S.; Tan, X.; Xue, Z.; Geysens, P.; Pan, H.; Guo, W.; Zhou, Z.; Zhang, X.; Vankelecom, I. F. J.; Fransaer, J. Cathodic Deposition-Assisted Synthesis of Thin Glass MOF Films for High-Performance Gas Separations. *Angew. Chem.* **2024**, *136*, No. e202401817.

https://doi.org/10.1021/acsomega.5c00466
ACS Omega 2025, 10, 7441−7451